Textile-to-mortar bond behavior: An analytical study

Ali Dalalbashi[1], Bahman Ghiassi[2], Daniel V. Oliveira[3]

ABSTRACT

Reliable design and application of textile-reinforced mortar (TRM) composites for the repair of existing masonry and concrete structures requires a fundamental understanding of the textile-to-mortar bond behavior as one of the main mechanisms controlling their nonlinear response and cracking behavior. It means suitable test setups and analytical models are needed to extract the bond-slip laws from the experimental pull-out tests. This paper proposes a new bond-slip law and analytical model, which predicts the bond behavior of lime and cement-based TRM composites considering the slip hardening and softening effects observed in experimental tests. For this purpose, the pull-out response of experimental specimens with different fiber types (steel and glass fibers), bond lengths, and mortar age are analyzed, and their bond slip-laws are extracted. The accuracy of the developed model is shown by comparing the analytical and experimental results.

Keywords: Textile reinforced mortar; Pull-out test; Analytical modeling; Fiber/matrix bond; Bond-slip law

---

[1] PhD Student, ISISE, Department of Civil Engineering, University of Minho, Guimarães, Portugal. E-mail: alidalalbashi@gmail.com
[2] Assistant Professor, Centre for Structural Engineering and Information, Faculty of Engineering, University of Nottingham, Nottingham, United Kingdom. E-mail: bahman.ghiassi@nottingham.ac.uk
[3] Associate Professor, ISISE, Department of Civil Engineering, University of Minho, Guimarães, Portugal. E-mail: danvco@civil.uminho.pt

1 Introduction

Textile reinforced mortar (TRM), also referred as Fabric Reinforced Cementitious Matrix (FRCM) in the literature, composites have received recent extensive attention for seismic strengthening of existing masonry and concrete structures [1–3]. The TRM composites composed of continuous fabrics embedded in an inorganic matrix (e.g., lime and cement) present several advantages comparing to conventional fiber-reinforced polymers. These include better compatibility, sustainability, breathability, and the capability of accommodating structural movements [4–6]. However, inorganic mortars do not have the same chemical compatibility with the reinforcement fibers.

TRM composites show good mechanical properties and a pseudo ductile response, making them suitable for seismic strengthening applications. This pseudo ductile response is owed to the fiber-to-mortar bond behavior, which itself is a function of fabric and mortar chemical, physical, and mechanical properties [7]. Understanding the fiber-to-mortar bond behavior and the affecting parameters are, therefore, of critical importance for the design and application of high-performance TRM composites. Despite this importance, most of the scientific attention has been given to the structural response of TRM composites or the structural components strengthened with TRMs [8–12]. Thus the existing literature on the fiber-to-mortar bond is very limited, especially with respect to lime-based TRMs commonly used for application to masonry structures [13–15]. However, the bond behavior of the short fiber and the cement-based matrix is available in the literature [16]. Consequently, several issues remain open regarding the characterization and modeling of this mechanism in the lime and cement-based TRM composites.

Pull-out tests are the most commonly used experimental [17,18] setups to evaluate fiber-to-mortar bond behavior. These tests allow measurement of the force-slip curves, which, with the support of analytical or numerical modeling approaches, can be used to extract suitable bond-slip laws [18,19]. However, the results obtained from different test setups diverge due to the differences in the boundary conditions introduced to the samples (which are poorly measured), which should be taken into account to extract the bond-slip laws. Also, a range of analytical modeling approaches for analysis of the pull-out test results and extraction of the bond-slip laws can be found in the literature [20–22]. Depending on the analytical modeling approach used, the extracted bond-slip laws obtained from the same pull-out tests can differ [18,19].

In a previous study, the authors developed an analytical model, based on Naaman et al. [20], for extraction of the bond-slip laws of TRM composites under both pull-pull and pull-push test setup configurations [18]. Although the accuracy of the previously proposed model to predicting pull-out response was perfect at the linear and nonlinear stage [18], this model was not suitable for predicting the slip hardening effect observed after the peak load in the tested TRM composites. However, the post-pick behavior is essential in the pseudo ductile response, and modeling of this stage will help to develop a comprehensive bond-slip law model. In addition, the proposed model can predict the complete debonding point, which can be crucial at the designing stage of TRM composites.

This paper proposes a new bond-slip law and analytical model, which predicts the pull-out curves in the full experimental range of response. Bond-slip laws are extracted for two different TRM composites and with different embedded lengths. The accuracy of the extracted bond-slip laws is then shown by comparing the analytical pull-out curves with the experimental results. Additionally, the sensitivity of the proposed model to the modulus of elasticity of the mortar at different ages is examined. Finally, an attempt has been made to provide the bond strength by a coefficient of mortar compressive strength at different mortar age.

2 Experimental program

2.1 Materials under investigation and characterization tests

Materials consisted of two commercially available hydraulic lime-based mortars as the matrix. These mortars are referred to as M1 and M2 throughout this paper. M1 mortar is a high-ductility hydraulic lime mortar composed of hydraulic lime (NHL) and Eco-Pozzolan(Planitop HDM Restauro), while M2 mortar is a pure natural NHL 3.5 lime and mineral geobinder base (Kerakoll GeoCalce Fino). For details on the procedure followed for the preparation of the paste, the reader is referred to [19]. The average compressive and flexural strengths (tests performed following ASTM C109 [23] and EN 1015-11 [24], respectively) are experimentally obtained as 7.84 MPa (coefficient of variation: CoV= 4%) and 5.56 MPa (CoV= 10%), respectively, for the M1 mortar, and as 8.89 MPa (CoV= 5%) and 2.33 MPa (CoV= 9%), respectively, for the M2 mortar.

Elastic modulus of the M1 and M2 mortars are tested according to EN 12390-13 [25] and are equal to 7182 MPa (CoV= 8%) and 9286 MPa (CoV= 6%), respectively, while these values reported by the manufacturers are 8000 MPa and 9000 MPa.

The reinforcing materials are glass and steel fibers. The glass fiber is a woven biaxial fabric mesh made of alkali-resistance fiberglass (Mapegrid G220). Its mesh size and area per unit length are equal to 25×25 mm^2 and 35.27 mm^2/ m, respectively. The steel fiber is a unidirectional ultra-high tensile steel sheet (GeoSteel G600), with a density of 670 g/m^2, an effective area of one cord (five wires) equal to 0.538 mm^2. Experimental direct tensile tests performed on five individual yarns shows average tensile stress, Young's modulus, and rupture strain of 2972 MPa (CoV= 8 %), 189.34 GPa (CoV= 8 %), and 0.0188 mm/mm (CoV= 9 %), respectively, for the steel fibers, and of 875 MPa (CoV= 13 %), 65.94 GPa (CoV= 5 %), and 0.0177 mm/mm (CoV= 10 %), respectively, for the glass fibers [19].

The mortar-fiber pairs correspond to the commercially available solution: glass fibers with M1 mortar and steel fibers with M2 mortar.

2.2 Pull-out specimens and test setup

The single-sided pull-out test setup developed in [18] is used in this study for studying the fiber-to-mortar bond performance. The specimens consist of single fibers embedded in the cuboid disk-shaped mortars with a cross-section of 125×16 mm^2. The fiber-free length is embedded in an epoxy resin block over a length of 200 mm and with a rectangular cross-sectional area of 10×16 mm^2, see Fig. 1. The specimens consist of steel cords are embedded in M2 mortar with embedded lengths of 150 mm. The glass yarns are embedded in M1 mortar with a 50 mm bond length. These selected embedded lengths are equal to the effective bond length of the steel and the glass fibers, as reported in [19]. Also, for investigating the effect of bond length on the bond-slip law, the pull-out response of a previous study conducted by authors is used [19], in which the steel-based TRMs were embedded in M2 mortar in 50, 100, 150, and 200 mm bond length.

Moreover, for investigating the effect of elastic modulus at different mortar age on the textile-to-mortar bond behavior, the experimental pull-out results presented in [14] are utilized. In that study [14], the pull-out responses of the steel and the glass-based TRM embedded in M2 and M1 mortar, respectively, were presented at 15, 30, 90, and 180 days. The bond length of steel-based TRM was 150 mm, while for the glass system was 50 mm.

The pull-out tests are carried out using a servo-hydraulic system with a maximum capacity of 25 kN and at a displacement rate of 1.0 mm/min. Two LVDTs, with a 20 mm range and 2-μm sensibility, are used to measure the slip at the loaded end of the samples. One LVDT is also used at the free end of the steel-based and glass-based samples with an embedded length of 150 mm and 50 mm, respectively, see Fig. 1.

3 Pull-out mechanism and response

The experimental load-slip curves of pull-out tests, see Fig. 2, usually consist of a linear elastic stage, section OA where the bond is perfect and elastic, and a progressive nonlinear debonding stage, section AB, which continues until reaching the peak load (P_P). Finally, after point C, a dynamic (or slippage) stage in which frictional bond is the only resisting mechanism at the interface [13,26,27]. The transition from the progressive debonding stage to the dynamic stage can either be smooth and upward or a sudden drop in the pull-out force if the frictional bond is smaller than the adhesive bond [26,28,29]. The pull-out load corresponding to point C (in this case, P_f) represents the total frictional force resisted by the system [13,30]. In the dynamic stage, a constant ($\beta = 0.0$), a slip hardening ($\beta > 0.0$), or a slip softening ($\beta < 0.0$) can be observed [29,31–35]. Slip hardening occur when the frictional stress between the fiber and the mortar increase due to the shape of fiber, embedded length, and the abrasion effect [21,32].

A range of analytical and numerical modeling approaches has been proposed and used in the literature to simulate the pull-out response or extraction of the bond-slip laws from the experimental pull-out curves. The shear lag models, such as the one proposed by Naaman et al. [20,36], are among the most commonly used techniques as they provide a realistic explanation of the debonding phenomenon by considering both adhesive and friction bond effects [37,38]. The authors have used the model proposed by Naaman et al. [20] in a previous publication to extract the bond-slip laws for the TRM systems tested under both pull-pull and pull-push test setup configurations [18]. However, this model was not suitable for predicting the slip hardening effect observed after the peak load in the tested TRM composites (cases where $\beta > 0.0$ in Fig. 2). To resolve that problem, this paper presents a novel bond-slip law for lime-based TRMs (though the proposed model can be used for the cement-based mortar), which allows predicting the full range of the pull-out response of those composites. This shape of bond-slip law, which is proposed based on Lin and Li [21] for the short fiber (at the range of 13 mm), is presented in Fig. 3. The analytical solution to the pull-out problem is consequently modified and briefly described next.

3.1 Basic equations

The static equilibrium of the tests, as shown in Fig. 4, requires that the applied load at the loaded end of the fiber, P, at any section, be equal to the sum of the local forces resisted by the fiber (F) and the mortar (M). Therefore, in a pull-push configuration, one has F= -M. Meanwhile, the free-body diagram of the embedded length of the textile in the mortar (Fig. 4) leads to:

$$\tau = \frac{dF}{\psi dx} \qquad (1)$$

where ψ and τ are the perimeter of the yarn and the shear stress at the yarn-to-mortar interface, respectively.

3.2 Bond-behavior in the elastic stage

Within the elastic stage, the local shear stress (τ) is related to the local slip (S) and follows a linear stress-slip relationship (Fig. 4):

$$\tau = \kappa S \qquad (2)$$

where κ is the bond shear modulus. As explained in [18], the mathematical formulation of the pull-out response is calculated by a second-order differential equation derived based on two equations of equilibrium, an equation of compatibility, and Hooke's law. This differential equation is expressed as follows:

$$\frac{d^2F}{dx^2} - \psi\kappa FQ = 0 \Rightarrow \frac{d^2F}{dx^2} - \lambda^2 F = 0 \quad \text{(3)}$$

in which Q and λ read:

$$\lambda = \sqrt{\kappa\psi Q}, \; Q = \frac{1}{A_f E_f} + \frac{1}{A_m E_m} \quad \text{(4)}$$

A and E are the cross-sectional area and Young's modulus, respectively (the subscripts f and m refer to the fiber and the mortar, respectively).

At each stage of the tests, the force at the free end is zero ($F_{(x=0)}=0$), and at the loaded end is the applied pull-out load ($F_{(x=L)}=P$). Imposing these two boundary conditions to Eq. (3) allows obtaining the solution to the differential equation:

$$\tau = \frac{dF}{\psi dx} = \frac{d}{dx}\left(P\frac{\sinh(\lambda x)}{\sinh(\lambda L)}\right) = \frac{P\lambda}{\psi} \times \frac{\cosh(\lambda x)}{\sinh(\lambda L)} \quad \text{(5)}$$

At the boundary of the elastic stage, the pull-out load is (Fig. 3):

$$P_{crit} = \frac{\tau_{max}\psi \tanh(\lambda L)}{\lambda} \quad \text{(6)}$$

where, P_{crit} is the critical force corresponding to the first debonding point occured at the loaded end, and τ_{max} is the bond (shear) strength. The slip at x= L is also equal to [18]:

$$S = \left(\frac{1}{\tanh(\lambda L)} - \frac{1}{\sinh(\lambda L)}\right)\frac{QP}{\lambda} \quad \text{(7)}$$

The slip corresponding to this critical force is obtained by imposing the value of P_{crit} from Eq. (6) into Eq. (7).

3.3 Bond-behavior in the nonlinear stage

Once the applied load reaches the P_{crit}, debonding at the loaded end initiates. The debonding length (u) increases as the applied slip to the system increases [20]. Along this length, the interfacial shear stress is equal to the frictional stress (the frictional shear strength, τ_f, on the bond slip-law), while the rest of the embedded length (L-u) is still perfectly bonded, as shown in Fig. 3. The total applied force resisted by the yarn can be expressed as P_b+ P_d, in which P_b and P_d are the bonded and debonded force.

The corresponding load along the debonding length (u) is express as $P_d = \tau_f \psi u$. On the other hand, applying the boundary conditions at the free end ($F_{(x=0)}=0$), and the loaded end ($F_{(x=L-u)}=P-P_d$) of the fiber to Eq. (3) allows obtaining shear stress at the nonlinear stage:

$$F=\left(P-\tau_f\psi u\right)\frac{\sinh\left(\lambda x\right)}{\sinh\left(\lambda\left(L-u\right)\right)} \quad \text{.....(8)}$$

$$\tau=\frac{dF_x}{\psi dx}=\frac{d}{\psi dx}\left[\frac{\left(P-\tau_f\psi u\right)\sinh\left(\lambda x\right)}{\sinh\left(\lambda\left(L-u\right)\right)}\right]=\frac{\left(P-\tau_f\psi u\right)\lambda\cosh\left(\lambda x\right)}{\psi\sinh\left(\lambda\left(L-u\right)\right)} \quad \text{.....(9)}$$

The maximum shear stress and the pull-out force in the nonlinear stage at the bonded length, x= L-u in Eq. (9), are equal to:

$$\tau_{max}=\frac{\left(P-\tau_f\psi u\right)\lambda}{\psi\tanh\left(\lambda\left(L-u\right)\right)} \quad \text{.....(10)}$$

$$P=P_b+P_d=\frac{\psi\tau_{max}}{\lambda}\tanh\left(\lambda\left(L-u\right)\right)+\tau_f\psi u \quad \text{.....(11)}$$

Furthermore, its corresponding slip at the nonlinear stage is:

$$S=\frac{Qu\left(2P-\tau_f\psi u\right)}{2}+\frac{Q\left(P-\tau_f\psi u\right)}{\lambda\tanh\left(\lambda\left(L-u\right)\right)}-\frac{Q\left(P-\tau_f\psi u\right)}{\lambda\sinh\left(\lambda\left(L-u\right)\right)} \quad \text{.....(12)}$$

3.4 Bond-behavior in the dynamic stage

Once the debonding has occurred along all the embedded length (u=L), the dynamic stage starts. In this stage, with an increment of the rigid body displacement/slip of the yarn, v, the embedded length decreases to L-v, which is under frictional stresses [20,39]. The pull-out force at this stage can, therefore, be calculated as [20]:

$$P = \tau_f \psi (L - v) \quad (13)$$

The load obtained from Eq. (13) is reduced linearly by increasing the rigid body displacement of the yarn (v). To model the slip hardening effect at this stage, a simple two-parameter phenomenological model proposed by Lin and Li [21] is adopted (Fig. 3). By considering suitable coefficients, it is possible to change the output of Eq. (13) from the linear curve to the nonlinear curve and model the slip hardening effect as follow:

$$P = \tau_f (L - \eta v)\left(1 + \beta \frac{L - \eta v}{d_f}\right)\psi \quad (14)$$

where η reflects the changes in the slope of the pull-out curve, β is the slip hardening coefficient, and d_f is the yarn diameter. Both η and β need to be determined by curve fitting procedure to achieve the best match with the experimental force-slip curves. In Eq. (14), the η sign is the opposite of the experimental load-slip curve slope, which means if the slope in the load-slip curve is positive, the η sign is negative, and vice versa. The local force in the fiber at a distance x (from zero and L-v) can, therefore, be calculated as:

$$F = \tau_f (L - \eta v - x)\left(1 + \beta \frac{L - \eta v - x}{d_f}\right)\psi \quad (15)$$

The total slip at the end of the fiber is defined as follow:

$$S = Q\int_0^{L-v} F_x \, dx \quad (16)$$

Replacing F_x from Eq. (15) into Eq. (16) gives the slip corresponding to the dynamic stage, S_{dyn}, as:

$$S_{dyn} = Q\tau_f \psi (L - v)\left\{L - \eta v - \frac{L-v}{2} + \frac{\beta}{d_f}\left[(L-\eta v)^2 + \frac{(L-v)^2}{3} - (L-\eta v)(L-v)\right]\right\} \quad (17)$$

In a particular case, where no slip hardening is considered (β= 0.0 and η =1.0), Eq. (17) will be reduced to:

$$S_{dyn} = Q\tau_f \psi \frac{(L-v)^2}{2} \quad (18)$$

This equation, Eq. (18), is the same as proposed in Sueki et al. [39] and Mobasher [40] for calculating the slip corresponding to the dynamic stage. Thus, the total slip in the dynamic stage is [39,40]:

$$S_{measured} = S_{dyn} + S_{nonlinear,\, last} + v \quad (19)$$

where $S_{nonlinear,\, last}$ is the last slip calculated in the nonlinear stage.

3.5 Pull-out simulation

The proposed analytical modeling can be used to extract the bond-slip laws and also to predict the pull-out response. The data necessary to run the analytical modeling is the mechanical and the geometric properties of the yarn and the mortar, as well as the experimental load-slip curves. The modulus of elasticity of the M1 and M2 mortar are 8 GPa and 9 GPa (taken from the technical datasheets), respectively. The modulus of elasticity for the glass and the steel fibers is equal to 65.94 GPa and 189.34 GPa (obtained from experimental tests), respectively. The steel and the glass fibers cross-section area (A_f) are equal to 0.538 mm^2 and 0.882 mm^2, respectively. The fiber perimeter and diameter are calculated from the cross-section area, assuming a circular cross-section.

The cross-section area of the mortar around yarns (A_m), which becomes active and participates in the debonding process, is a critical parameter in the analytical results. Since this parameter cannot be measured using conventional experimental testing methods, it is usually obtained based on a parametric study and considering the convergence of the numerical solution [18]. Based on the previous studies performed by the authors [18], it was found that the effective mortar area can be considered as $A_m = \alpha A_f = 55A_f$ for the steel-based TRM. For the glass-based TRM, α is considered as 7.5. These α values are derived by performing the try and error method. It means a primary value for α is considered, and the model is run. If the accurate answer is obtained, the effective mortar area will be accepted; otherwise, a new value will be considered for α. The accurate answer is obtained if the three following conditions will reach: i: solving the differential equations presented in sections 3.2 and 3.3, ii: having the full debonding length less than embedded length ($u<L$), iii: having slip corresponding to τ_{max} less than the relative slip of the fiber under conditions of full debonding, $S_0 = QL^2\tau_f\psi/2$. It should be mentioned that the considerable difference between α values (55 and 7.5 for the steel and the glass fibers) is resulted from both the fiber properties (E_f and A_f) and the obtaining accurate answer process as mentioned above.

4 Results and discussion

4.1 Pull-out response in two TRM composites

Fig. 5 presents the experimental pull-out response envelope, obtained from four tested steel based-TRM specimens, together with the analytical extracted bond-slip laws and analytical predicted load-slip curves. The main parameters of the experimental pull-out curves and analytically extracted bond-slip laws are also presented in Table 1 and Table 2. For the development of the analytical pull-out curves, the experimental pull-out curves of individual samples are initially used to extract the bond-slip laws using the analytical model adopted in this study. These bond-slip laws are then used for modeling the presented analytical pull-out curves.

The agreement between the experimental and analytical pull-out curves of the steel-based TRM is clear (Fig. 5 and Fig. 6). The initial stiffness, post-peak slip hardening effect, and final deterioration of the bond strength are all simulated with excellent accuracy. It can also be observed that the proposed analytical model is suitably able to predict the slip at the free end of the samples (Fig. 6). The experimental results show that the dynamic stage initiates near the peak load, Fig. 6. This observation is also predicted with perfect accuracy (an error of less than 1%) with the proposed analytical model, see Table 2. This observation also shows that the dynamic stage initiation could be assumed to occur at the peak load with reasonable accuracy and previously considered in the literature [13,26,41]. The predicted load and slip (representative of the end of the nonlinear stage and beginning of the dynamic stage), as well as the difference among the results of analytical and experimental debonding loads, are presented in the last three columns of Table 2. It can be observed that the analytical predictions of the debonding load have a good agreement with the experimental results so that the average difference is equal to 0.1 % (see Table 2).

The envelope of the experimental load-slip curves of the glass-based TRM specimens is shown in Fig. 7. The individual results obtained from each sample, together with the main extracted information from the experimental results, are also presented in Table 3. A more considerable variation in the experimental results is observed compared to the steel-based TRM results, which may be attributed to the telescopic behavior of the glass fiber [42–44] and the abrasion effect [21,35] by breaking down layer by layer of filaments. The drop in the force after the peak load (corresponding to the lower frictional resistance compared to the adhesive resistance in this system) followed by a slip hardening behavior is also observed in this TRM system. Again, the analytical predictions have a perfect agreement with the experimental results regarding both loaded and free end slip predictions (Fig. 8). Here also, the complete debonding occurs near the peak load (Fig. 8, Table 3). The results show that the debonding load is also predicted with outstanding accuracy with an error of 0.2% (Table 4).

It is interesting that although the glass-based TRM specimens had a smaller embedded length, they show a mean value of the slip hardening coefficient (β=0.0031) of about ten times that of the steel fibers (Table 4 and Table 2).

4.2 Effect of embedded length in steel-based TRM

The proposed analytical model is used here to extract the bond-slip laws of the steel-based TRM samples with different bond lengths presented in [14,19]. It should be noted that these samples were tested at the 60-day curing ages and had embedded lengths of 50, 100, 150, and 200 mm. The envelopes of the experimental results and the pull-out response details of individual samples are presented in Fig. 9 and Table 5. The results indicate that by increasing the embedded length, the peak load, and its corresponding slip increase, while the initial stiffness decreases, which is in line with other studies [39,45].

The bond-slip laws are extracted from the individual samples and then averaged for each embedded length (see Fig. 10 and Table 6). These bond-slip laws are then used for predicting the load-slip curves following two different approaches (predicted load-slip curves are shown in Fig. 9, together with experimental envelopes). (i) The average bond-slip law corresponding to each embedded length is used to predict the load-slip curve of that embedded length. (ii) The average bond-slip law obtained from 150 mm embedded length samples (that is believed larger than the effective embedded length [7,14]) is used for predicting the load-slip curves of all embedded lengths. This second approach is followed to evaluate the accuracy of the hypothesis that the bond-slip laws obtained from pull-out tests performed on samples with embedded lengths higher than the effective bond length are sufficient for predicting the bond behavior in all other embedded lengths.

Table 6 reports the bond-slip laws for different bond lengths (approach i). Table 6 shows that by increasing the embedded length, the frictional shear strength (τ_f) and the bond shear modulus (slope of the linear part, κ) decrease. Meanwhile, the slip hardening coefficient (β) and the bond strength (τ_{max}) increase. Specimens with 200 mm bond length show a decrement of bond strength owing to their different pull-out responses at the debonding point. A comparison among the load-slip curves of experimental results shows the intensity of the load drop in 200 mm bond length is the least, which means the debonding force is slightly higher than the frictional resistance after debonding [46]. This hypothesis can be supported by investigating the strain distribution along the steel fibers, as shown in Fig. 11. From Fig. 11, the maximum strain of fiber with 200 mm bond length at the end of the linear and nonlinear stages is 0.206 % and 0.223 %, respectively. While for other bond lengths, it is between 0.255 and 0.3 %. Furthermore, Yamao et al. [47] reported that the bond stress-slip relationships in the short and long bond length are significantly different [48]. It can be deduced that the bond in the specimens with 200 mm embedded length is governed more by the friction stress rather than the bond strength.

The predictions of the pull-out curves when using the bond-slip laws from 150 mm embedded length are also in excellent agreement with the experimental results in most regions of the pull-out curves (the predictions are only slightly higher in 200 mm embedded length).

4.3 Effect of mortar age

The proposed analytical model is also utilized to extract the bond-slip laws and the analytical load-slip curves of the steel and the glass-based TRM samples at different mortar age. The experimental envelope curves and the pull-out response details of individual samples are presented in Fig. 12, Fig. 13, and Table 7. The results show that by increasing the mortar age, the bond parameters of glass-based TRM increase, while for the steel-based, the bond properties increase firstly, and after 30 days, decreases [14].

For obtaining the bond-slip laws, firstly, the elastic modulus of mortars at each age is calculated based on their compressive strength (f'_c):

$$E_{m,f'_c} = \xi\sqrt{f'_c} \qquad (20)$$

Since the elastic modulus of the mortars is tested only at 90 days, ξ is obtained at this age, and then it is used for calculating $E_{m,f'c}$ at different ages. Table 8 shows both f'_c and $E_{m,f'c}$ of the M1 and M2 mortars at different mortar ages. The bond-slip laws extracted from the average of the experimental load-slip curves are presented in Fig. 14, and the bond-slip law parameters for individual specimens are presented in

Table 9 and Table 10. These bond-slip laws are then used for predicting the load-slip curves, as shown in Fig. 12, Fig. 13.

The results of steel-based TRM illustrate that the bond strength (τ_{max}), the frictional stress (τ_f), and the bond modulus (κ) increase until 30 days, and after this point, these parameters decrease, which are in line with the compressive strength of M2 mortar (see Table 8 and

Table 9). However, the slip hardening (β) increases until 30 days and remains approximately constant after this point. On the other hand, the τ_{max}, κ, and β of the glass-based TRM show an increasing trend until 90 days, and then these parameters decrease dramatically. However, τ_f shows a different trend by increasing until 180 days, as shown in Table 10. Furthermore, a comparison of a ratio of the bond strength (τ_{max}) to the frictional stress (τ_f) shows that this ratio increases by increasing the age of M2 mortar. In contrast, glass-based TRM shows the opposite behavior.

Table 11 compares the effect of mortar elastic modulus on the bond strength and the frictional stress at different mortar ages, which are the average of individual specimens. It can be observed that τ_{max} and τ_f of the steel-based TRM obtained with $E_{m, f'c}$ is around 3.02~5.05 MPa and 1.34~1.69 MPa representing a 2~16% and 1~2% error to the bond parameters obtained by $E_{m, m}$ (see Table 11). However, τ_{max} and τ_f of the glass-based TRM shows 37~66% and 22~51% error, respectively.

One possibility way for the initial estimation of the bond strength is to use the compressive strength of the matrix [49]. Fig. 15 displays the changes in the bond strength ratio (τ_{max}) to the mortar compressive strength (f'_c) at the different mortar ages. The mean value of τ_{max}/ f'_c of the steel-based TRM varies between 0.34 and 0.54, with an average of 0.43 (CoV= 15%). While for the glass-based TRM is between 0.28 and 0.81 with an average of 0.47 (CoV= 39%). Although the results scatter is large, given that the lime-based mortar strength changes with age (unlike cement showing almost constant resistance after 28 days), these results can be used as a preliminary estimate.

5 Conclusions

Aiming at better predicting the pull-out test results, a new bond-slip law was proposed in this paper. The proposed bond-slip law was implemented in a shear lag analytical model for simulation of the pull-out response. The solution to the analytical model was also modified for better consideration of the pull-out response in the dynamic stage. The following conclusions can be drawn from the presented study:

- The proposed bond-slip law and analytical solution can predict the pull-out response of a range of TRM composites considering the slip hardening and softening effect observed in the experimental results.
- The experimental results showed that in both glass- and steel-based TRMs (studied here), full debonding (corresponding to the initiation of the dynamic stage in the bond behavior) occurs near the peak load. This information is vital for the solution of the differential equations used for the extraction of the bond-slip laws when free-end measurements are not available. This observation proves the hypothesis that the dynamic stage starts when the embedded length completely debonded ($u= L$).
- It was also observed that the bond-slip laws extracted from pull-out tests performed on samples with embedded lengths higher than the effective embedded length (in this case 150 mm embedded length for the steel-based TRM) can be directly used for prediction of the bond behavior in samples with other embedded lengths. This observation is essential as it provides a base for designing test programs to evaluate the bond-slip laws in TRM composites.
- The results showed that though the mortar elastic modulus did not affect the bond-slip law of steel-based TRM, it caused the bond-slip law parameters of the glass-based TRM to change. Besides, using mechanical properties of mortar (such as compressive strength) can be useful only for estimating the bond strength, especially when using lime-based mortar.
- This study was performed at the micro-level to understand the behavior of TRM/ FRCM composites. It is the beginning step for investigating TRM behavior at the structural level

and the real service conditions by strengthening the existing masonry and concrete structures.

Acknowledgments

This work was partly financed by FEDER funds through the Competitivity Factors Operational Program (COMPETE) and by national funds through the Foundation for Science and Technology (FCT) within the scope of the project POCI-01-0145-FEDER-007633. The support to the first author through grant SFRH/BD/131282/2017 is acknowledged. Besides, the authors would like to thank the Kerakoll Company for supplying the GeoCalce Fino mortar as well as GeoSteel G600 fibers.

6 References

[1] R. Allahvirdizadeh, D. V. Oliveira, R.A. Silva, Numerical modeling of the seismic out-of-plane response of a plain and TRM-strengthened rammed earth subassembly, Eng. Struct. 193 (2019) 43–56. https://doi.org/10.1016/j.engstruct.2019.05.022.

[2] F. Graziotti, U. Tomassetti, A. Penna, G. Magenes, Out-of-plane shaking table tests on URM cavity walls, Eng. Struct. 125 (2016). https://doi.org/10.1016/j.engstruct.2016.07.011.

[3] L.A.S. Kouris, T.C. Triantafillou, State-of-the-art on strengthening of masonry structures with textile reinforced mortar (TRM), Constr. Build. Mater. 188 (2018) 1221–1233. https://doi.org/10.1016/j.conbuildmat.2018.08.039.

[4] S. Barr, W.J. McCarter, B. Suryanto, Bond-strength performance of hydraulic lime and natural cement mortared sandstone masonry, Constr. Build. Mater. 84 (2015) 128–135. https://doi.org/10.1016/j.conbuildmat.2015.03.016.

[5] A. Moropoulou, A. Bakolas, P. Moundoulas, E. Aggelakopoulou, S. Anagnostopoulou, Strength development and lime reaction in mortars for repairing historic masonries, Cem. Concr. Compos. 27 (2005) 289–294. https://doi.org/10.1016/j.cemconcomp.2004.02.017.

[6] J. Lanas, J.I. Alvarez, Masonry repair lime-based mortars: Factors affecting the mechanical behavior, Cem. Concr. Res. 33 (2003) 1867–1876. https://doi.org/10.1016/S0008-8846(03)00210-2.

[7] B. Ghiassi, D. V Oliveira, V. Marques, E. Soares, H. Maljaee, Multi-level characterization of steel reinforced mortars for strengthening of masonry structures, Mater. Des. 110 (2016) 903–913. https://doi.org/10.1016/j.matdes.2016.08.034.

[8] E. Grande, G. Milani, Numerical simulation of the tensile behavior of FRCM strengthening systems, Compos. Part B Eng. (2020) 107886. https://doi.org/10.1016/J.COMPOSITESB.2020.107886.

[9] S. De Santis, F. Ceroni, G. de Felice, M. Fagone, B. Ghiassi, A. Kwiecień, G.P. Lignola, M. Morganti, M. Santandrea, M.R. Valluzzi, A. Viskovic, Round Robin Test on tensile and bond behaviour of Steel Reinforced Grout systems, Compos. Part B Eng. 127 (2017) 100–120. https://doi.org/10.1016/j.compositesb.2017.03.052.

[10] E. Grande, G. Milani, Interface modeling approach for the study of the bond behavior of FRCM strengthening systems, Compos. Part B Eng. 141 (2018) 221–233. https://doi.org/10.1016/j.compositesb.2017.12.052.

[11] N. Ismail, J.M. Ingham, In-plane and out-of-plane testing of unreinforced masonry walls strengthened using polymer textile reinforced mortar, Eng. Struct. 118 (2016) 167–177. https://doi.org/10.1016/j.engstruct.2016.03.041.

[12] X. Wang, C.C. Lam, V.P. Iu, Experimental investigation of in-plane shear behaviour of grey clay brick masonry panels strengthened with SRG, Eng. Struct. 162 (2018) 84–96. https://doi.org/10.1016/j.engstruct.2018.02.027.

[13] D.L. Naik, A. Sharma, R.R. Chada, R. Kiran, T. Sirotiak, Modified pullout test for indirect characterization of natural fiber and cementitious matrix interface properties, Constr. Build. Mater. 208 (2019) 381–393. https://doi.org/10.1016/j.conbuildmat.2019.03.021.

[14] A. Dalalbashi, B. Ghiassi, D. V. Oliveira, Textile-to-mortar bond behaviour in lime-based textile reinforced mortars, Constr. Build. Mater. 227 (2019) 116682. https://doi.org/10.1016/j.conbuildmat.2019.116682.

[15] J. Jiang, C. Jiang, B. Li, P. Feng, Bond behavior of basalt textile meshes in ultra-high ductility cementitious composites, Compos. Part B Eng. 174 (2019) 107022. https://doi.org/10.1016/j.compositesb.2019.107022.

[16] M. Zhu, J. Zhu, T. Ueda, M. Su, F. Xing, A method for evaluating the bond behavior and anchorage length of embedded carbon yarn in the cementitious matrix, Constr. Build. Mater. 255 (2020) 119067. https://doi.org/10.1016/j.conbuildmat.2020.119067.

[17] B. Ghiassi, Mechanics and durability of textile reinforced mortars: a review of recent advances and open issues, RILEM Tech. Lett. 4 (2019) 130–137. https://doi.org/10.21809/rilemtechlett.2019.99.

[18] A. Dalalbashi, B. Ghiassi, D.V. Oliveira, A. Freitas, Effect of test setup on the fiber-to-mortar pull-out response in TRM composites: experimental and analytical modeling, Compos. Part B Eng. 143 (2018) 250–268. https://doi.org/10.1016/j.compositesb.2018.02.010.

[19] A. Dalalbashi, B. Ghiassi, D.V. Oliveira, A. Freitas, Fiber-to-mortar bond behavior in TRM composites: effect of embedded length and fiber configuration, Compos. Part B Eng. 152 (2018) 43–57. https://doi.org/10.1016/j.compositesb.2018.06.014.

[20] A.E. Naaman, G.G. Namur, J.M. Alwan, H.S. Najm, Fiber pullout and bond slip. i: analytical study, J. Struct. Eng. 117 (1991) 2769–2790. https://doi.org/10.1061/(ASCE)0733-9445(1991)117:9(2769).

[21] Z. Lin, V.C. Li, Crack bridging in fiber reinforced cementitious composites with slip-hardening interfaces, J. Mech. Phys. Solids. 45 (1997) 763–787. https://doi.org/10.1016/S0022-5096(96)00095-6.

[22] B. Banholzer, Analytical simulation of pull-out tests- the direct problem, Cem. Concr. Compos. 27 (2005) 93–101. https://doi.org/10.1016/j.cemconcomp.2004.01.006.

[23] ASTM C109/C109M-05, Standard test method for compressive strength of hydraulic cement mortars (Using 2-in. or [50-mm] Cube Specimens), 2005.

https://doi.org/10.1520/C0109_C0109M-05.

[24] BS EN 1015-11, Methods of test for mortar for masonry. Determination of flexural and compressive strength of hardened mortar, 1999.

[25] BS EN 12390-13, Testing hardened concrete. Determination of secant modulus of elasticity in compression, 2013.

[26] Z. Lin, T. Kanda, V.C. Li, On interface property characterization and performance of fiber reinforced cementitious composites, J. Concr. Sci. Eng. RILEM. 1 (1999) 173–184. http://hdl.handle.net/2027.42/84718.

[27] E.A. Schauffert, G. Cusatis, Lattice discrete particle model for fiber-reinforced concrete. I: Theory, J. Eng. Mech. 137 (2011) 826–833. https://doi.org/10.1061/(ASCE)EM.

[28] E.A. Schauffert, G. Cusatis, D. Pelessone, J.L. O'Daniel, J.T. Baylot, Lattice discrete particle model for fiber-reinforced concrete. II: Tensile fracture and multiaxial loading behavior, J. Eng. Mech. 138 (2011) 834–841. https://doi.org/10.1061/(asce)em.1943-7889.0000392.

[29] V.C. Li, H.-C. Wu, Y.-W. Chan, Effect of plasma treatment of polyethylene fibers on interface and ementitious composite properties, J. Am. Ceram. Soc. 79 (1996) 700–704. https://doi.org/10.1111/j.1151-2916.1996.tb07932.x.

[30] C. DiFrancia, T.C. Ward, R.O. Claus, The single-fibre pull-out test. 1: Review and interpretation, Compos. Part A Appl. Sci. Manuf. 27 (1996) 597–612. https://doi.org/10.1016/1359-835X(95)00069-E.

[31] W.P. Boshoff, V. Mechtcherine, G.P.A.G. van Zijl, Characterising the time-dependant behaviour on the single fibre level of SHCC: Part 1: Mechanism of fibre pull-out creep, Cem. Concr. Res. 39 (2009) 779–786. https://doi.org/10.1016/j.cemconres.2009.06.007.

[32] C. Redon, V.C. Li, C. Wu, H. Hoshiro, T. Saito, A. Ogawa, Measuring and modifying interface properties of PVA fibers in ECC matrix, J. Mater. Civ. Eng. 13 (2001) 399–406. https://doi.org/10.1061/(ASCE)0899-1561(2001)13:6(399).

[33] K.H. Tsai, K.S. Kim, The micromechanics of fiber pull-out, J. Mech. Phys. Solids. 44 (1996) 1147–1159. https://doi.org/10.1016/0022-5096(96)00019-1.

[34] V.C. Li, H.C. Wu, Y.W. Chan, Interfacial property tailoring for pseudo strain- hardening cementitious composites, Adv. Technol. Des. Fabr. Compos. Mater. Struct. Eng. Appl. Fract. Mech. 14 (1995) 261–268. https://doi.org/10.1007/978-94-015-8563-7_18.

[35] Y. Wang, V.C. Lf, S. Backer, Modelling of fibre pull-out from a cement matrix, Int. J. Cem. Compos. 10 (1988) 143–149. https://doi.org/10.1016/0262-5075(88)90002-4.

[36] A.E. Naaman, G.G. Namur, J.M. Alwan, H.S. Najm, Fiber pullout and bond slip. ii: experimental validation, J. Struct. Eng. 117 (1991) 2791–2800. https://doi.org/10.1061/(ASCE)0733-9445(1991)117:9(2791).

[37] H. Stang, Z. Li, S.P. Shah, Pullout problem: stress versus fracture mechanical approach, J. Eng. Mech. 116 (1990) 2136–2150. https://doi.org/10.1061/(ASCE)0733-9399(1990)116:10(2136).

[38] S. Zhandarov, E. Mäder, An alternative method of determining the local interfacial shear strength from force-displacement curves in the pull-out and microbond tests, Int. J. Adhes. Adhes. 55 (2014) 37–42. https://doi.org/10.1016/j.ijadhadh.2014.07.006.

[39] S. Sueki, C. Soranakom, B. Mobasher, M. Asce, A. Peled, Pullout-slip response of fabrics embedded in a cement paste matrix, J. Mater. Civ. Eng. 19 (2007) 718–728. https://doi.org/10.1061/(ASCE)0899-1561(2007)19:9(718).

[40] B. Mobasher, Mechanics of Fiber and Textile Reinforced Cement Composites, Taylor & Francis Group, London- New York, 2012.
[41] J. Alwan, A.E. Naaman, P. Guerrero, Effect of mechanical clamping on the pull-out response of hooked steel fibers embedded in cementitious matrices, Concr. Sci. Eng. 1 (1999) 15–25. http://rilem.net/gene/main.php?base=600026&id_publication=391&id_papier=7278.
[42] B. Banholzer, Bond of a strand in a cementitious matrix, Mater. Struct. 39 (2006) 1015–1028. https://doi.org/10.1617/s11527-006-9115-y.
[43] X. Shilang, L. He, Bond properties and experimental methods of textile reinforced concrete, J. Wuhan Univ. Technol. Mater. Sci. Ed. 22 (2007) 529–532. https://doi.org/10.1007/s11595-006-3529-9.
[44] A. J. Majumdar, A.J. Majumdar, The role of the interface in glass fibre reinforced cement, Cem. Concr. Res. 4 (1974) 247–266. https://doi.org/10.1016/0008-8846(74)90137-9.
[45] B. Banholzer, Bond behaviour of a multi-filament yarn embedded in a cementitious matrix, RWTH Aachen University, 2004. https://doi.org/10.1017/CBO9781107415324.004.
[46] W.P. Boshoff, V. Mechtcherine, G.P.A.G. van Zijl, Characterising the time-dependant behaviour on the single fibre level of SHCC: Part 2: The rate effects on fibre pull-out tests, Cem. Concr. Res. 39 (2009) 787–797. https://doi.org/10.1016/j.cemconres.2009.06.006.
[47] H. Yamao, L. Chou, J. Niwa, Experimental study on bond stress slip relationship, in: Japan Soc. Civ. Eng., 1984: pp. 219–228.
[48] S. Hong, S.K. Park, Uniaxial bond stress-slip relationship of reinforcing bars in concrete, Adv. Mater. Sci. Eng. 2012 (2012). https://doi.org/10.1155/2012/328570.
[49] Bond of reinforcement in concrete: State-of-the-art report, Lausanne : International Federation for Structural Concrete (fib), 2000. https://doi.org/10.35789/fib.BULL.0010.

Table 1. Pull-out response parameters for steel-based TRMs (embedded length of 150 mm).

Specimen	Slip corresponding to peak load [mm]	Peak load [N]	Initial stiffness [N/mm]	Debonding slip [mm]	Debonding load [N]
1	0.80	634.8	1210.8	0.80	634.8
2	0.80	802.5	1339.9	0.80	802.5
3	0.85	766.0	1455.6	0.75	729.3
4	0.81	759.0	1103.3	0.81	759.0
Average ***CoV (%)***	0.81 (3)	740.6 (9)	1277.4 (10)	0.79 (3)	731.4 (8)

Table 2. Analytical bond-slip laws and predicted debonding load/slip for steel-based TRM (embedded length of 150 mm).

Specimen	τ_{max} [MPa]	τ_f [MPa]	κ [MPa/mm]	β	Debonding slip [mm]	Debonding load [N]	Error in debonding load prediction [%]
1	2.55	1.17	3.83	0.0003	0.74	626.5	1.3
2	3.51	1.51	6.05	0.0003	0.94	795.1	0.9
3	3.47	1.55	7.88	0.0003	0.87	761.4	-4.4
4	2.67	1.44	1.97	0.0003	0.85	745.8	1.7
Average ***CoV (%)***	3.05 (15)	1.42 (10)	4.93 (45)	0.0003 (0)	0.85 (8)	732.2 (9)	-0.1

Table 3. Pull-out response parameters for glass-based TRMs (embedded length of 50 mm).

Specimen	Slip corresponding to peak load [mm]	Peak load [N]	Initial stiffness [N/mm]	Debonding slip [mm]	Debonding load [N]
1	0.32	274.0	4015.4	0.32	274.0
2	0.34	218.3	2954.4	0.34	218.3
3	0.14	202.2	1639.3	0.14	202.2
4	0.28	273.0	2028.2	0.28	273.0
5	0.33	237.9	4166.3	0.33	237.9
Average ***CoV (%)***	0.28 (26)	241.1 (12)	2659.3 (34)	0.28 (26)	241.1 (12)

Table 4. Analytical bond-slip laws and predicted debonding load/slip for glass-based TRM (embedded length of 50 mm).

Specimen	τ_{max} [MPa]	τ_f [MPa]	K [MPa/mm]	β	Debonding slip [mm]	Debonding load [N]	Error in debonding load prediction [%]
1	6.61	1.03	174.36	0.0017	0.32	273.6	0.1
2	3.94	0.87	92.86	0.0044	0.25	218.2	0.0
3	2.38	0.76	22.48	0.0032	0.23	202.2	0.0
4	4.19	0.78	41.66	0.0031	0.36	272.6	0.1
5	4.86	1.08	187.79	0.0053	0.26	236.7	0.5
Average ***CoV (%)***	4.4 (31)	0.90 (14)	103.83 (65)	0.0035 (34)	0.28 (17)	240.7 (12)	0.2

Table 5. Pull-out response parameters for steel-based TRMs with different embedded lengths [19].*

Bond length [mm]	Slip corresponding to peak load [mm]	Peak load [N]	Initial stiffness [N/mm]
50	0.23 (16)	406.8 (15)	3320.6 (1)
100	0.52 (7)	696.1 (5)	2940.5 (11)
150	1.08 (15)	992.5 (8)	2993.9 (16)
200	1.34 (6)	995.7 (2)	2424.3 (12)

* CoVs (%) presented in parentheses

Table 6. Bond-slip law parameters for the steel-based TRM with different embedded lengths.

Bond length [mm]	Specimen	τ_{max} [MPa]	τ_f [MPa]	κ [MPa/mm]	β
50	1	3.58	2.07	16.57	0.0001
	2	4.55	3.10	21.11	0.0001
	Average CoV (%)	***4.07 (12)***	***2.59 (20)***	***18.84 (12)***	***0.0001 (0)***
100	1	6.10	2.08	57.46	0.0002
	2	3.97	2.31	34.84	0.0002
	3	4.55	2.56	33.90	0.0002
	Average CoV (%)	***4.87 (18)***	***2.32 (8)***	***42.07 (26)***	***0.0002 (0)***
150	1	4.85	1.87	35.03	0.0003
	2	6.26	2.29	31.42	0.0003
	3	6.18	2.10	69.84	0.0003
	4	6.85	2.29	53.35	0.0003
	Average CoV (%)	***6.04 (12)***	***2.14 (8)***	***47.41 (32)***	***0.0003 (0)***
200	1	3.76	1.69	25.17	0.0004
	2	3.25	1.79	42.23	0.0008
	3	3.53	1.79	25.45	0.0003
	Average CoV (%)	***3.51 (6)***	***1.76 (3)***	***30.95 (26)***	***0.0005 (43)***

Table 7. Pull-out response parameters for steel and glass-based TRMs at different mortar age [14].*

Fiber and mortar	Age [days]	Slip corresponding to peak load [mm]	Peak load [N]	Initial stiffness [N/mm]
Steel fiber (150 mm embedded length) and mortar M2	15	0.8 (19)	720 (7)	2410 (43)
	30	0.9 (11)	871 (11)	2147 (33)
	90	0.8 (3)	740 (10)	1289 (17)
	180	0.9 (19)	730 (19)	1520 (31)
Glass fiber (50 mm embedded length) and mortar M1	15	2.6 (14)	284 (12)	482 (17)
	30	1.9 (36)	250 (35)	639 (31)
	90	2.3 (15)	378 (18)	856 (24)
	180	2.3 (31)	390 (14)	781 (20)

* CoVs (%) presented in parentheses

Table 8. Compressive strength and elastic modulus of M1 and M2 mortar.*

-	Age [days]	15	30	90	180
Mortar M1	f'_c [MPa]	5.91 (8)	7.07 (9)	7.84 (4)	7.46 (10)
	$E_{m,f'c}$ [MPa]	6233	6821	7182	7006
Mortar M2	f'_c [MPa]	8.76 (7)	9.53 (10)	8.89 (5)	7.48 (9)
	$E_{m,f'c}$ [MPa]	9215	9610	9286	8515

* CoVs (%) presented in parentheses, f'_c: mortar compressive strength reported at [14], $E_{m,\,f'c}$: Elastic modulus of the mortars calculated with f'_c.

Table 9. Bond-slip law parameters for the steel-based TRM at different mortar age (embedded length of 150 mm).

Age [day]	Specimen	τ_{max} [MPa]	τ_f [MPa]	κ [MPa/mm]	β
15	1	3.63	1.44	8.89	0.0001
	2	3.97	1.29	21.73	0.0001
	3	5.06	1.39	28.47	0.0001
	4	3.17	1.24	11.13	0.0001
	Average CoV (%)	***3.96 (18)***	***1.34 (6)***	***17.56 (45)***	***0.0001 (0)***
30	1	4.10	1.83	13.58	0.0002
	2	3.27	1.55	10.56	0.0004
	3	5.99	1.70	21.76	0.0004
	4	6.83	1.69	40.36	0.0005
	Average CoV (%)	***5.05 (28)***	***1.69 (6)***	***21.56 (54)***	***0.0004 (29)***
90	1	2.53	1.17	3.69	0.0003
	2	3.49	1.51	5.90	0.0003
	3	3.44	1.55	7.71	0.0003
	4	2.64	1.44	1.83	0.0003
	Average CoV (%)	***3.02 (15)***	***1.42 (10)***	***4.78 (46)***	***0.0003 (0)***
180	1	3.43	1.78	8.51	0.0006
	2	2.63	1.53	2.63	0.0003
	3	1.98	1.11	4.22	0.0006
	4	4.13	1.60	11.85	0.0003
	Average CoV (%)	***3.04 (27)***	***1.51 (16)***	***6.80 (53)***	***0.0005 (33)***

Table 10. Bond-slip law parameters for the glass-based TRM at different mortar age (embedded length of 50 mm).

Age [day]	Specimen	τ_{max} [MPa]	τ_f [MPa]	κ [MPa/mm]	β
15	1	2.93	0.93	6.13	0.0170
	2	1.97	0.85	6.11	0.0130
	3	2.76	0.98	8.30	0.0120
	4	1.73	0.75	7.34	0.0085
	Average ***CoV (%)***	***2.35*** ***(22)***	***0.88*** ***(10)***	***6.97*** ***(13)***	***0.0126*** ***(24)***
30	1	5.54	0.58	14.46	0.0490
	2	2.46	0.85	10.59	0.0030
	3	2.74	0.52	35.53	0.0150
	4	3.19	0.54	17.95	0.0200
	Average ***CoV (%)***	***3.48*** ***(35)***	***0.62*** ***(21)***	***19.63*** ***(49)***	***0.0218*** ***(78)***
90	1	5.03	1.18	17.14	0.0280
	2	4.59	0.55	14.20	0.0370
	3	9.45	0.60	37.64	0.0630
	4	8.85	0.44	42.06	0.0650
	Average ***CoV (%)***	***6.98*** ***(31)***	***0.69*** ***(41)***	***27.76*** ***(44)***	***0.0483*** ***(33)***
180	1	3.57	1.22	7.51	0.0080
	2	2.42	1.06	23.50	0.0020
	3	3.49	1.41	16.42	0.0076
	4	2.73	1.28	20.18	0.0160
	Average ***CoV (%)***	***3.05*** ***(16)***	***1.24*** ***(10)***	***16.90*** ***(35)***	***0.0084*** ***(59)***

Table 11. Effect of mortar Elastic Modulus on the bond strength and friction stress.

TRM system	Age [days]	τ_{max} [Mpa]			τ_f [Mpa]		
		$E_{m,\,m}$	$E_{m,\,f'c}$	$E_{m,\,m}/E_{m,\,f'c}$	$E_{m,\,m}$	$E_{m,f'c}$	$E_{m,\,m}/E_{m,\,f'c}$
Steel based (150 mm embedded length)	15	3.90	3.96	0.98	1.35	1.34	1.01
	30	4.22	5.05	0.84	1.71	1.69	1.01
	90	2.97	3.02	0.98	1.43	1.42	1.01
	180	2.78	3.04	0.91	1.54	1.51	1.02
Glass based (50 mm embedded length)	15	1.47	2.35	0.63	1.15	0.88	1.31
	30	3.53	3.48	1.01	0.64	0.62	1.03
	90	4.37	6.98	0.63	1.04	0.69	1.51
	180	5.08	3.05	1.66	0.97	1.24	0.78

$E_{m,\,m}$: mortar Elastic Modulus provided by manufactory, $E_{m,\,f'c}$: Elastic modulus of the mortars calculated with f'_c.

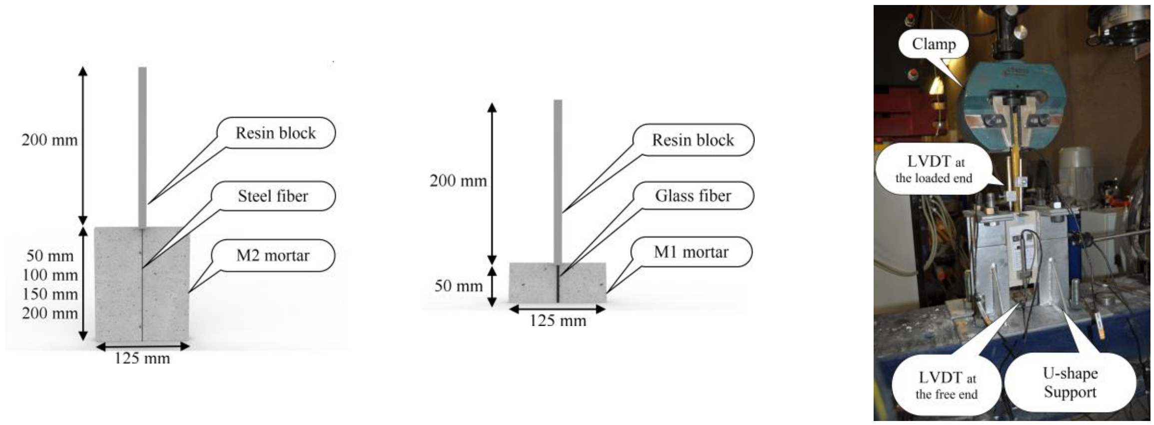

(a) (b) (c)

Fig. 1. Pull-out details: (a) and (b) specimens configuration; (c) test setup

.

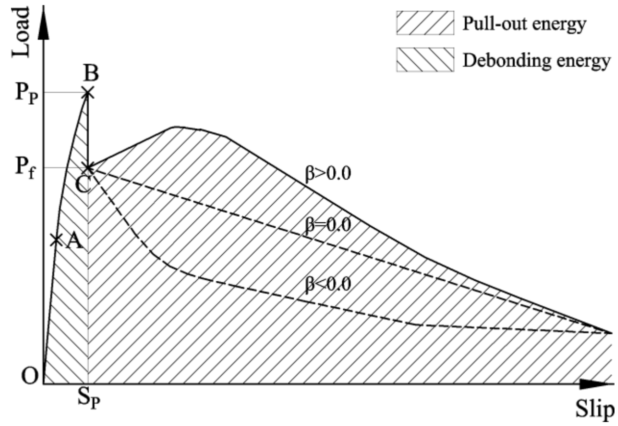

Fig. 2. Typical pull-out curves.

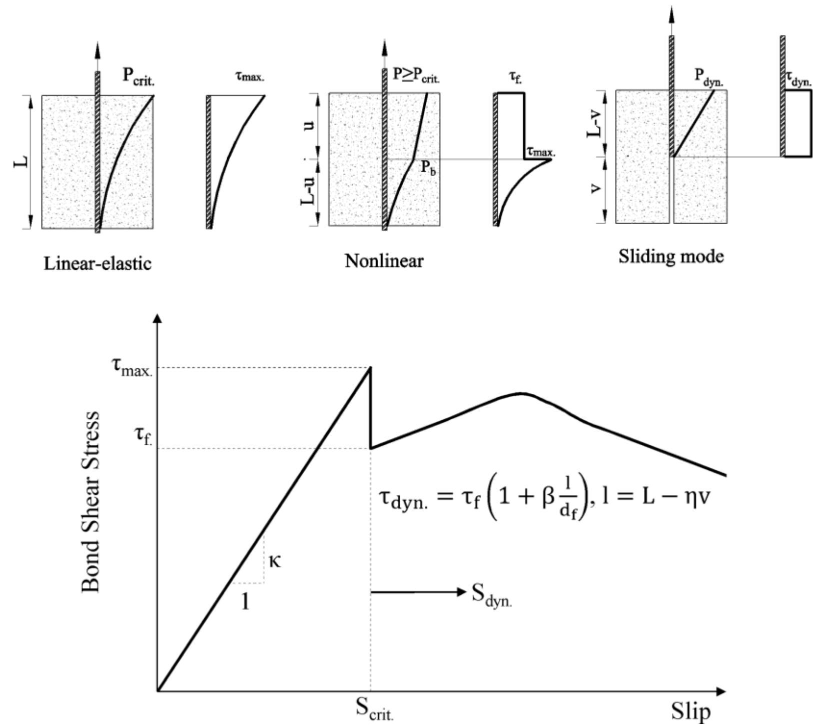

Fig. 3. Bond shear stress-slip, and force distribution along with the fiber at different pull-out stages.

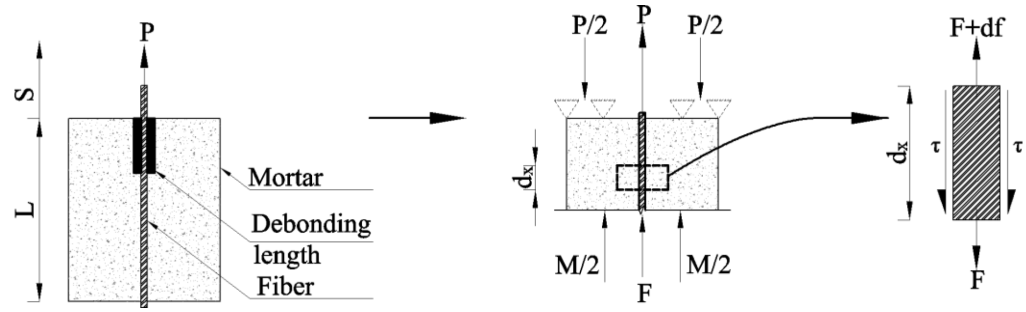

Fig. 4. Free-body diagram of a pull-push test, global force equilibrium, and infinitesimal segment of fiber.

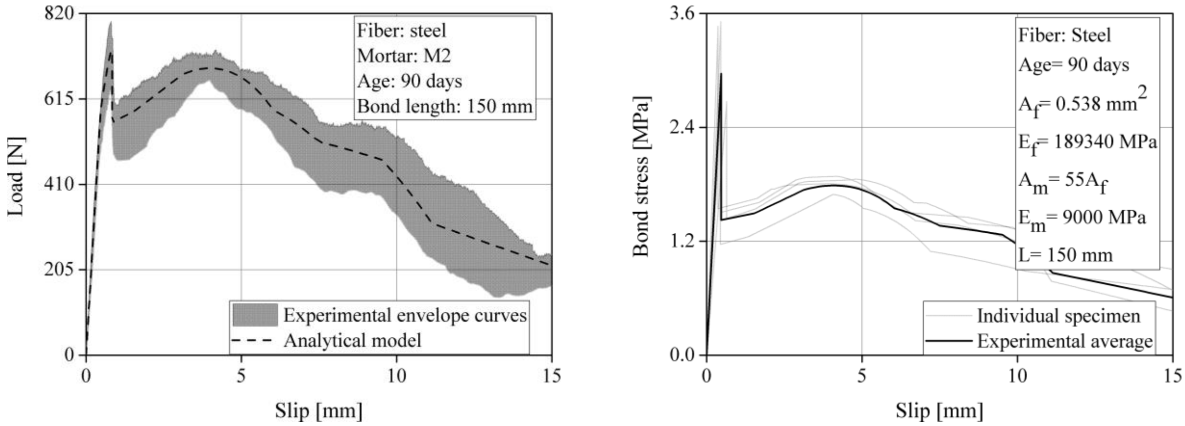

(a) (b)

Fig. 5. Steel-based TRM with 150 mm embedded length tested at 90 days (a) pull-out response; (b) analytical bond-slip law.

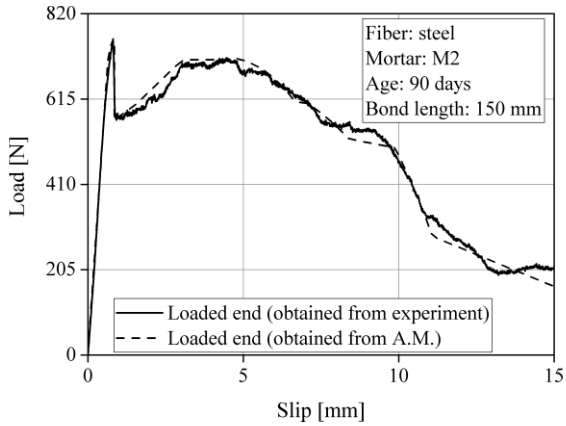

(a)

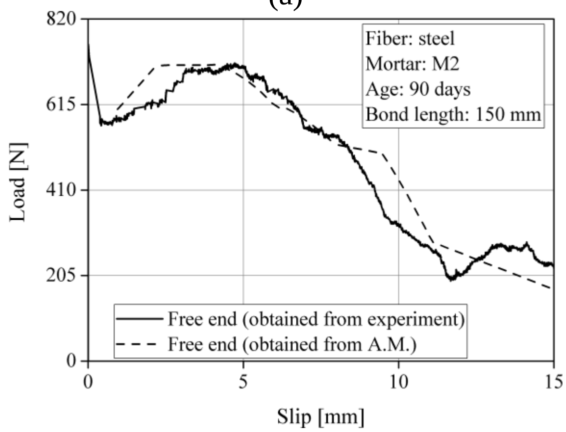

(b)

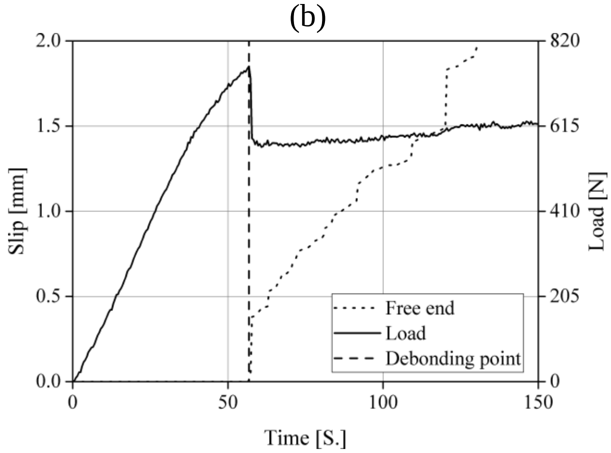

(c)

Fig. 6. The pull-out response of a steel-based TRM specimen: (a) loaded end slip curves; (b) free end slip curves (c) load-time vs. slip-time curves (A.M. stands for Analytical Modeling).

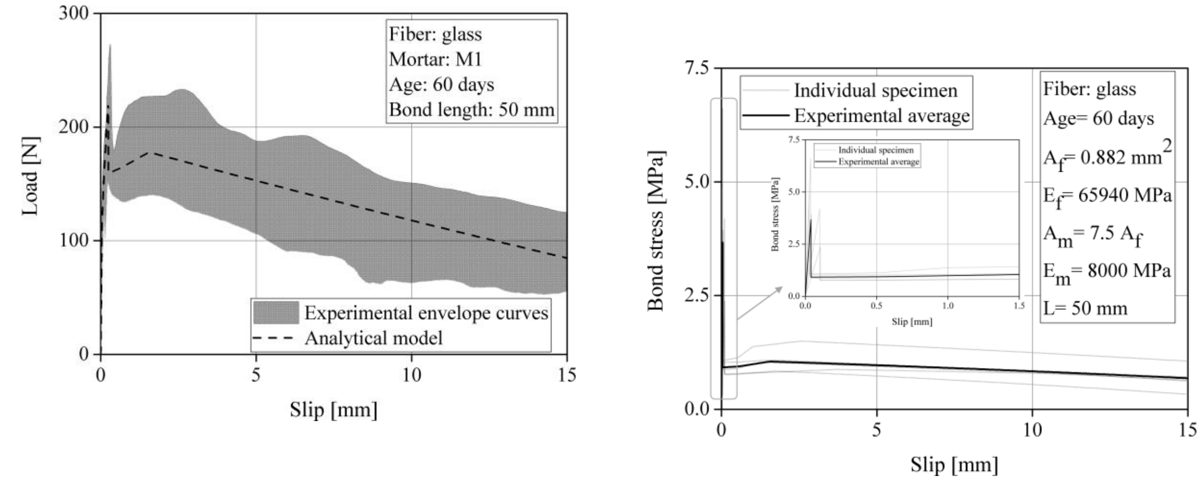

(a) (b)

Fig. 7. Glass-based TRM with 50 mm embedded length tested at 60 days (a) pull-out response; (b) analytical bond-slip law.

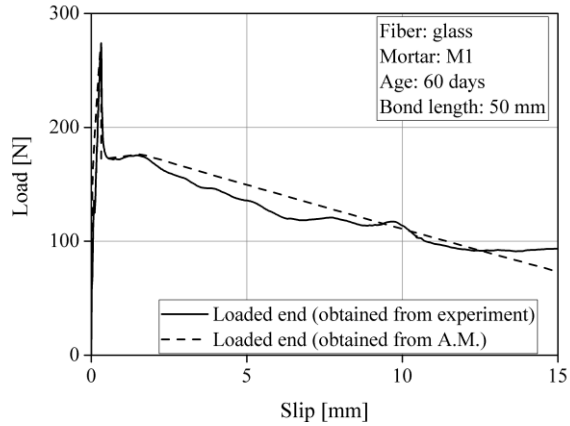

(a)

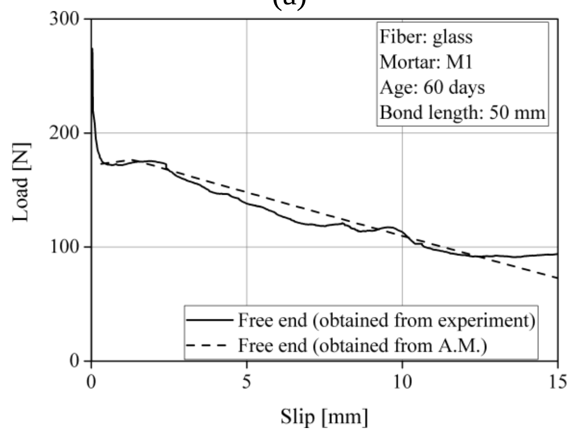

(b)

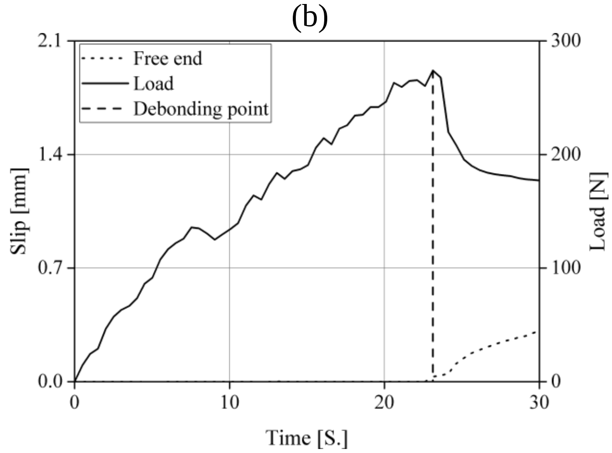

(c)

Fig. 8. The pull-out response of a glass-based TRM specimen: (a) loaded end slip curves; (b) free end slip curves (c) load-time vs. slip-time curves (A.M. stands for Analytical Modeling).

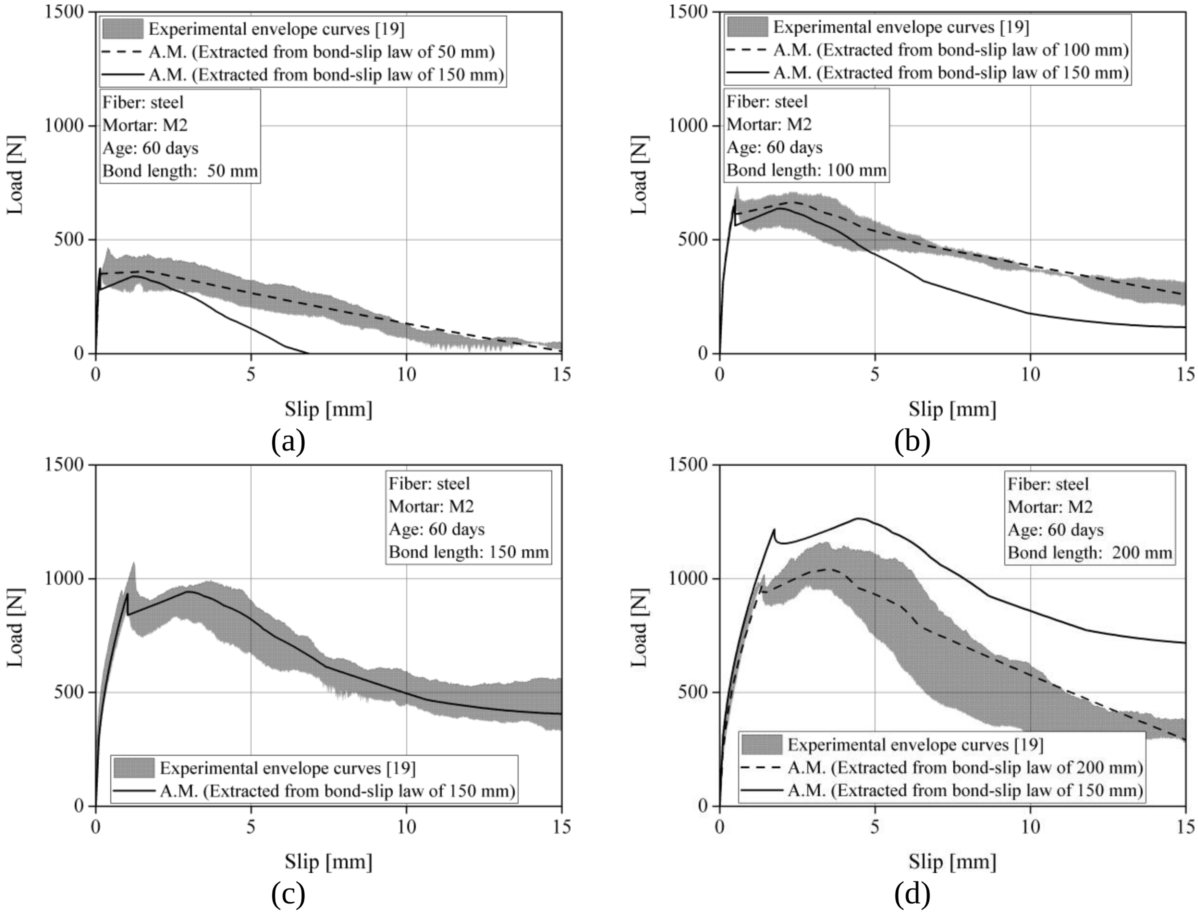

Fig. 9. The pull-out response of the steel-based TRM at 60 days: (a) 50 mm; (b) 100 mm; (c) 150 mm; (d) 200 mm bond length (A.M. stands for Analytical Modeling).

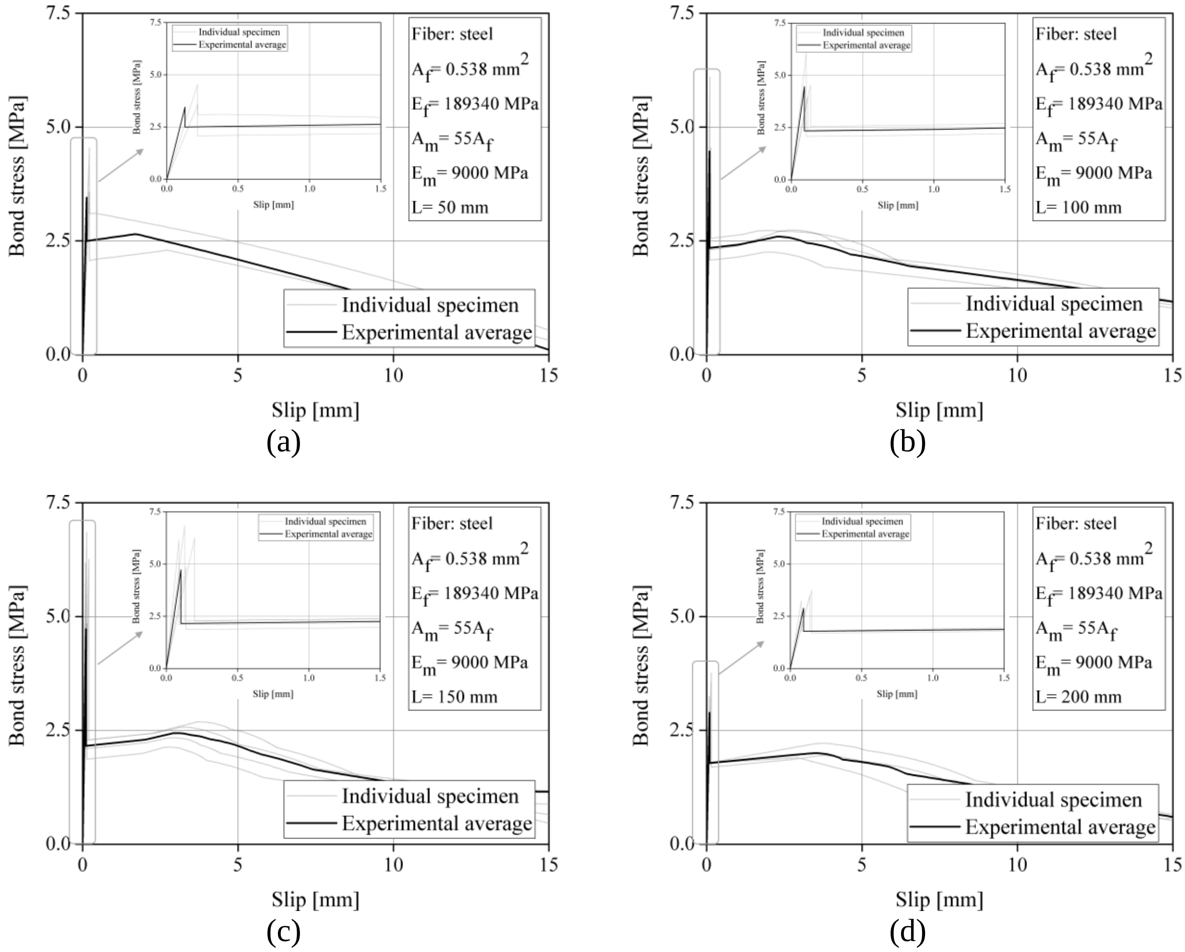

Fig. 10. The bond slip-law of the steel-based TRM at 60 days and in (a) 50 mm; (b) 100 mm; (c) 150 mm; (d) 200 mm bond length.

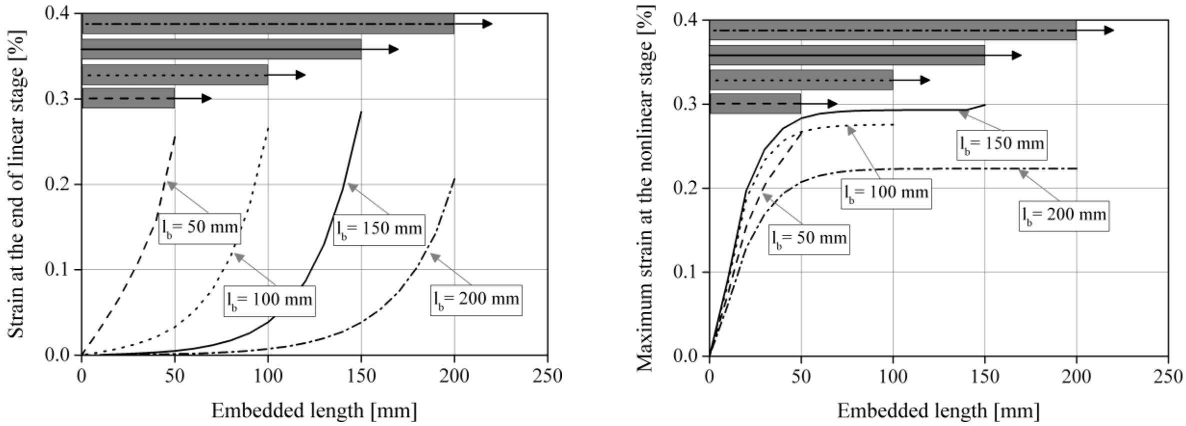

(a) (b)

Fig. 11. Fiber strain distributions along the embedded length of the steel-based TRM: (a) at the end of the linear stage; (b) at the nonlinear stage (l_b: bond length).

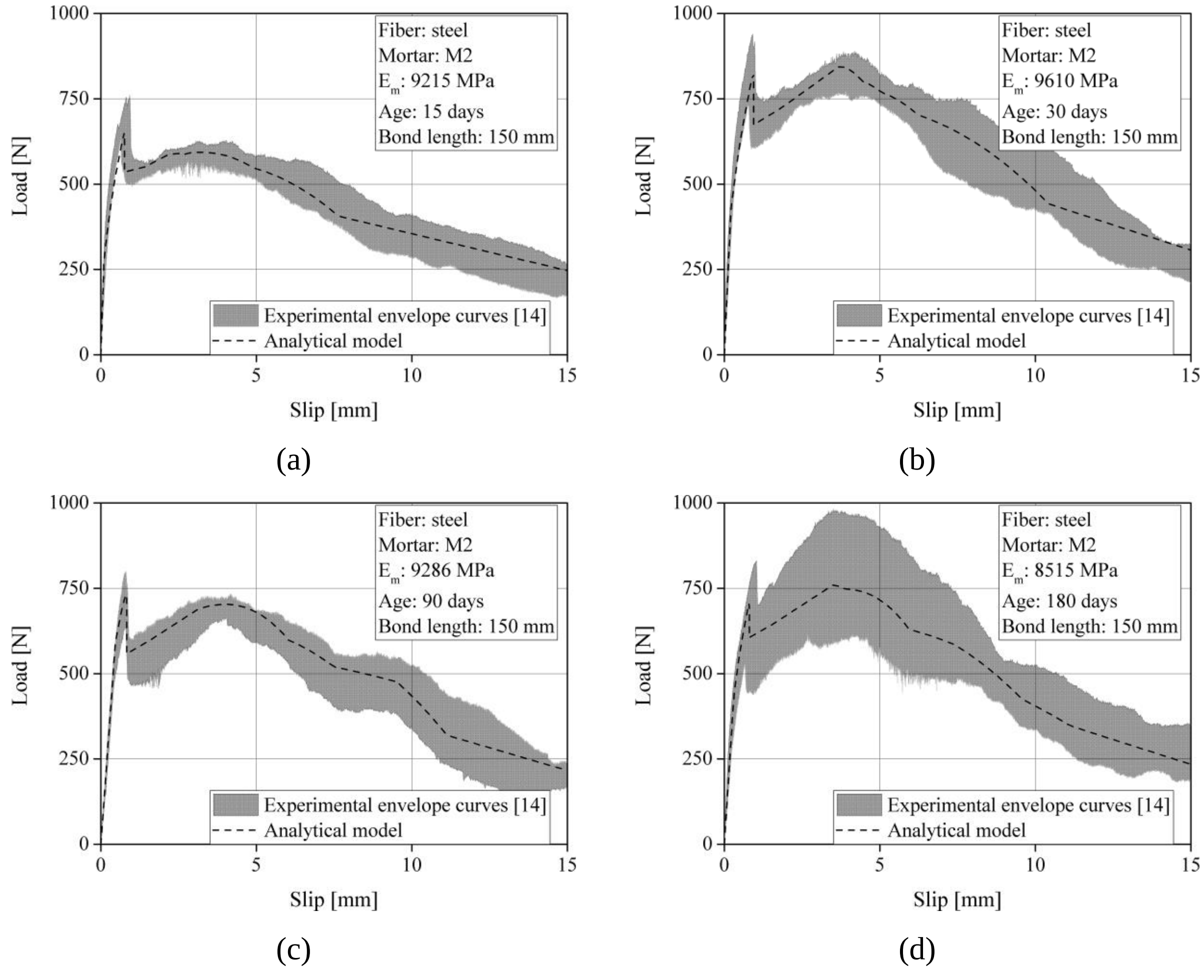

Fig. 12. The experimental and analytical pull-out response of the steel-based TRM at different mortar age: (a) 15-day; (b) 30-day; (c) 90-day; (d) 180-day ages.

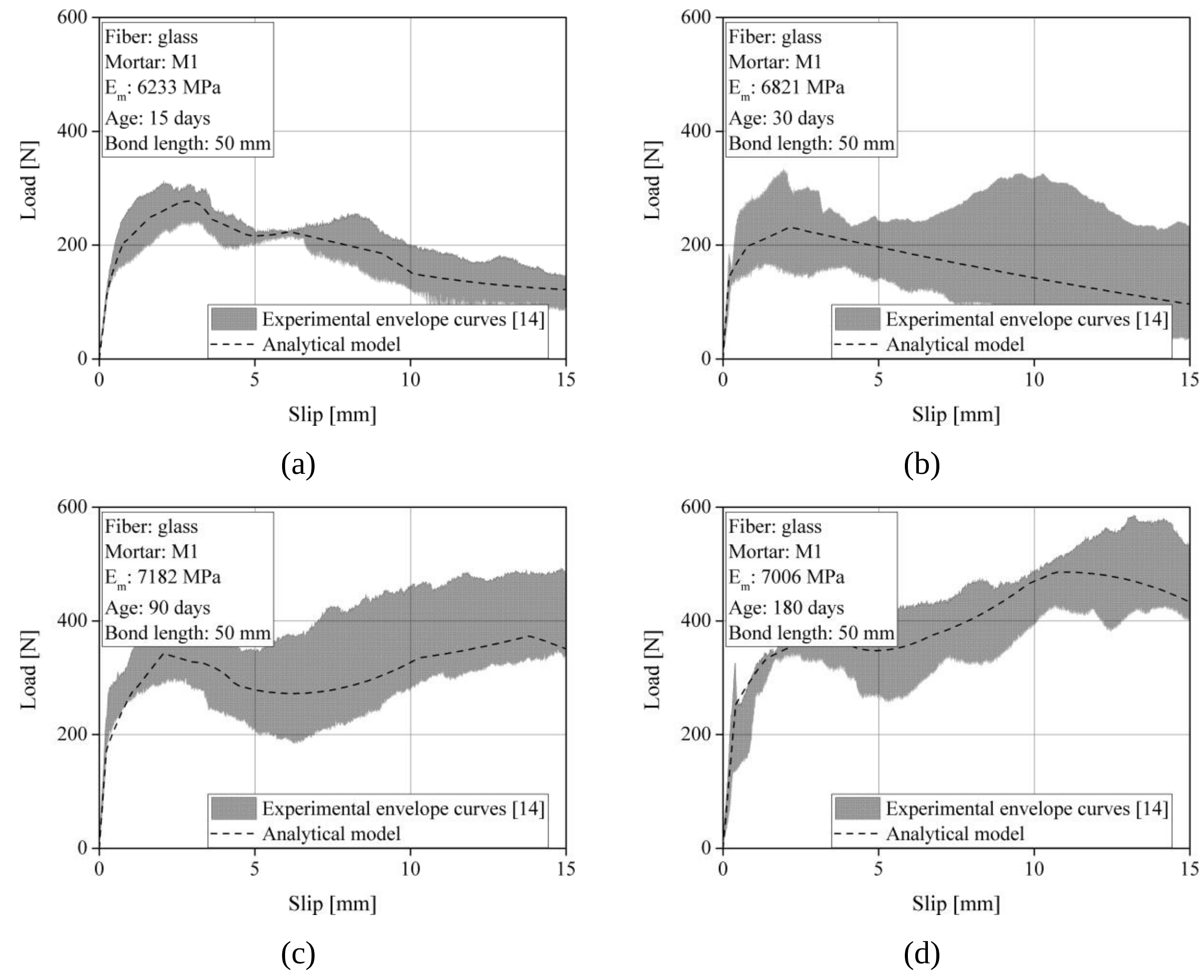

Fig. 13. The experimental and analytical pull-out response of the glass-based TRM at different mortar age: (a) 15-day; (b) 30-day; (c) 90-day; (d) 180-day ages.

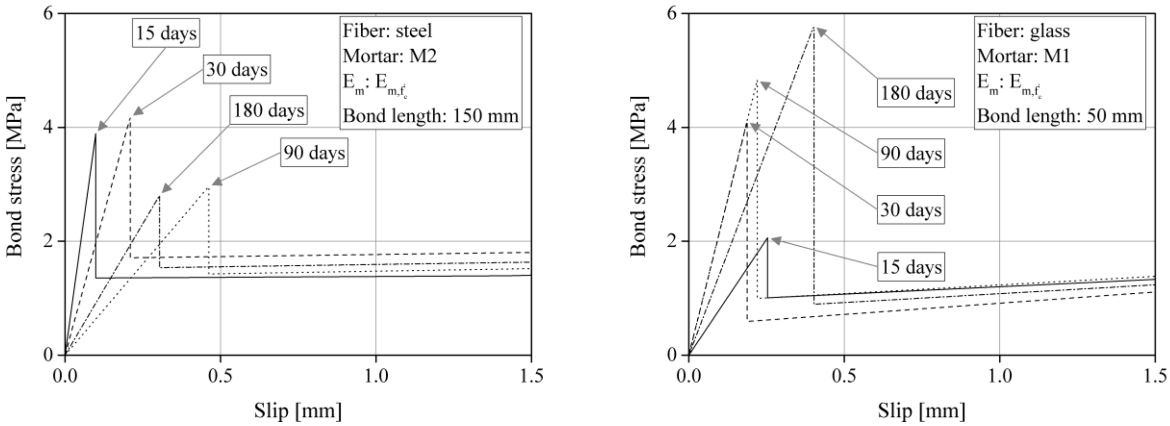

(a) (b)

Fig. 14. The average bond-slip law at different mortar age: (a) steel-based TRM; (b) glass-based TRM.

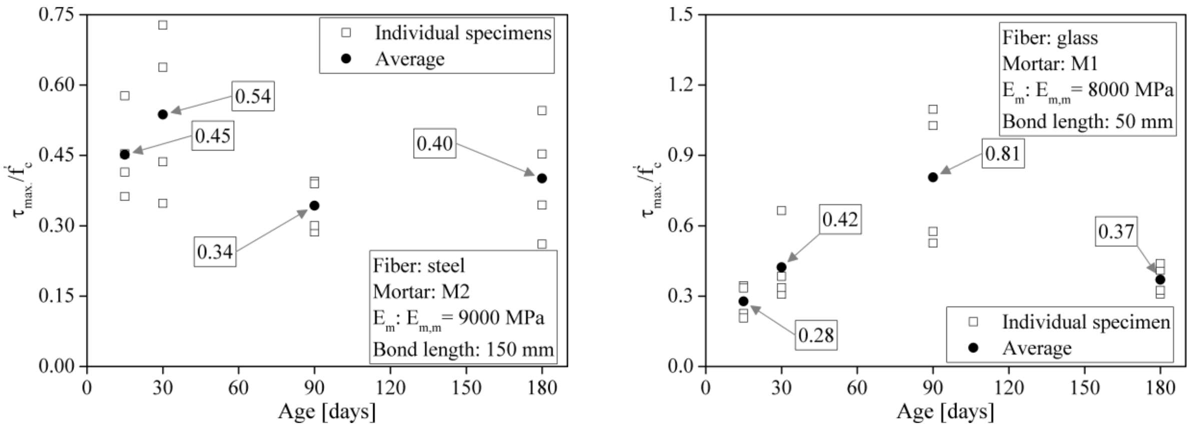

(a) (b)

Fig. 15. Changes in the bond strength to mortar compressive strength (τ_{max}/ f'_c) at different mortar age: (a) steel-based TRM and mortar M2; (b) glass-based TRM and mortar M1.